

# Ionization-Induced Subcycle Metallization of Nanoparticles in Few-Cycle Pulses

Qingcao Liu,<sup>1</sup> Lennart Seiffert,<sup>2</sup> Frederik Süßmann, Sergey Zharebtsov, Johannes Passig, Alexander Kessel, Sergei A. Trushin, Nora G. Kling, Itzik Ben-Itzhak, Valerie Mondes, Christina Graf, Eckart Rühl, Laszlo Veisz, Stefan Karsch, Jessica Rodríguez-Fernández, Mark I. Stockman, Josef Tiggesbäumker, Karl-Heinz Meiwes-Broer, Thomas Fennel,\* and Matthias F. Kling\*



Cite This: *ACS Photonics* 2020, 7, 3207–3215



Read Online

ACCESS |



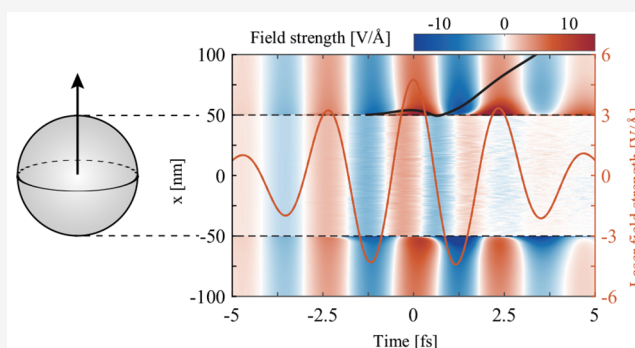
Metrics & More



Article Recommendations

**ABSTRACT:** Strong-field laser-matter interactions in nanoscale targets offer unique avenues for the generation and detailed characterization of matter under extreme conditions. Field-driven, subcycle ionization-induced metallization of nanoscale solids in intense laser fields has been predicted (Peltz et al. Time-Resolved X-ray Imaging of Anisotropic Nanoplasma Expansion. *Phys. Rev. Lett.* **2014**, *113*, 133401), but its observation was hampered by a lack of a smoking gun. Here, we report the ultrafast metallization of isolated dielectric and semiconducting nanoparticles under intense few-cycle laser pulses. The highest-energy electron emission is found to be a decisive proof that shows a characteristic cutoff modification to a metallic limit for intensities high enough to ignite carrier avalanching in the volume of the particles. Semiclassical Mean-field Mie Monte-Carlo transport simulations reveal the underlying dynamics and explain the observed evolution by near-field driven electron backscattering from the metallizing target.

**KEYWORDS:** *strong-field nanophysics, avalanche ionization*



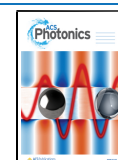
Controlled laser fields with only a few optical periods have enabled far-reaching insights into the physics of strong-field driven solids, including the mechanisms of high harmonic generation,<sup>1,2</sup> field-induced band gap reduction in semiconductors and insulators,<sup>3–5</sup> and control of macroscopic currents in dielectrics.<sup>6–8</sup> Besides the associated contributions from reversible interband polarization and transient intraband currents, persistent carrier generation and avalanching will ultimately dominate the nonlinear response at high intensity and are of major relevance in the context of plasma formation and laser (nano) machining.<sup>9–11</sup> Particularly challenging is the time-resolved characterization of plasma formation near the optical breakdown, as the relevant strong-field dynamics unfolds on subcycle time scales.

Clusters and nanoparticles represent a well-established platform for analyzing correlated and cooperative effects in strong-field near-infrared (NIR) laser-matter interactions and uncovered the importance of collective resonance excitation for the case of cluster nanoplasmas.<sup>12,13</sup> For rare gas clusters, nanoplasma formation is typically ignited by atomic strong-field ionization,<sup>14</sup> followed by rapid avalanche ionization that results in a hot, overdense plasma with a collective dipole mode (localized surface plasmon or Mie plasmon for spherical

particles) in the ultraviolet spectral range.<sup>15,16</sup> For nanotips, multi-MeV electron kinetic energies have been reported at ultrarelativistic intensity ( $10^{20}$  W/cm<sup>2</sup>).<sup>17</sup> The intensity threshold for triggering nanoplasma formation by NIR-induced strong-field ionization<sup>14,18</sup> can be lowered when generating seed electrons via single-photon ionization by an additional weak extreme ultraviolet pulse.<sup>19</sup> Upon expansion of the resulting overdense nanoplasma, the plasma density can drop to the value required for establishing resonance between the Mie plasmon and the NIR laser field. The resulting transient resonant excitation of the Mie plasmon can lead to extreme energy absorption<sup>12</sup> and high-energy electron emission via forward scattering within a single cycle in the plasmonically enhanced near-field.<sup>20,21</sup> This expansion-induced resonance is

Received: August 13, 2020

Published: October 23, 2020



well studied and typically established within a few hundred femtoseconds to a few picoseconds.<sup>15,16</sup>

The free electron density in an initially dielectric or semiconducting (i.e., nonmetallic) material, however, can also cross the value associated with the described resonance during the ionization-driven build-up phase of the nanoplasma. This early realization of the resonant density precedes the expansion-induced one, but lasts only fractions of an optical cycle, preventing the buildup of resonant enhancement.<sup>16,19</sup> This has so far hampered the observation of this early crossing of the resonant density. Importantly, this crossing of the resonant density can be associated with the transition from a nonmetallic to a metal-like response of the system. Here, the metal-like response refers to a nanoplasma with a high density of plasma electrons such that internal fields are essentially screened instantaneously like in the case of a perfect conductor. This situation is realized if the characteristic response time of the polarization, that is, the period of the collective oscillations of conduction electrons, is smaller than the period of the driving field. For a sphere, this condition for a quasi-instantaneous, metal-like response is fulfilled if the electron density exceeds the resonant density. So far, however, the ramifications of the metallization in the spectra of emitted electrons remain an open question.

Electron emission kinetic energy spectra and their cutoffs have been reported at low intensities (up to  $10^{13}$  W/cm<sup>2</sup>) for various nanotargets,<sup>22</sup> including isolated nanospheres,<sup>23–26</sup> nanotips,<sup>27–32</sup> and surface nanostructures.<sup>33</sup> For the case of nanoparticles, elastic electron backscattering at the surface was found to dominate the fast electron emission.<sup>23,24</sup> Additional modifications arise through nonlinear charge-interaction<sup>34–36</sup> and nanofocusing due to field-propagation.<sup>25</sup> In this intensity regime and for small SiO<sub>2</sub> spheres with negligible propagation effects, electron cutoff energies around  $50 U_p$  were found.<sup>23,24,26</sup> Here,  $U_p = \frac{e^2 E_0^2}{4m_e \omega_0^2}$  is the ponderomotive potential of the laser field  $E(t, \varphi_{ce}) = E_0(t) \cos(\omega_0 t + \varphi_{ce})$  at central frequency  $\omega_0$ , with elementary charge  $e$ , electron mass  $m_e$ , envelope function  $E_0(t)$  with field amplitude  $E_0$ , and carrier-envelope phase (CEP)  $\varphi_{ce}$ .

In this work, we study CEP-dependent electron kinetic energy spectra and analyze the characteristic cutoff signatures resulting from near-field enhanced electron acceleration in isolated nanospheres at intensities near and beyond the onset of the dielectric breakdown. We find a substantial departure from the previously reported cutoff behavior. Our generalized 3D-transport simulations for SiO<sub>2</sub> nanoparticles reveal the underlying subcycle electron dynamics and unambiguously assign a sudden change in electron cutoff energies to ionization-induced metallization. The conclusions from the combined experimental and theoretical work on SiO<sub>2</sub> nanoparticles are tested and confirmed with further experimental data for other dielectric, semiconducting, and metallic nanoparticles.

## EXPERIMENTAL TECHNIQUES

The experimental setup is shown schematically in Figure 1. Laser pulses of 4.5 fs duration centered at  $\lambda = 720$  nm were obtained from a Ti:Sa laser system extended with a neon-filled hollow-core fiber at a repetition rate of 1 kHz.<sup>37</sup> A fraction of the beam was split off and sent to a stereographic above-threshold-ionization (Stereo-ATI) phase meter for single-shot CEP measurement.<sup>38,39</sup> Here, the highest energy ATI electrons

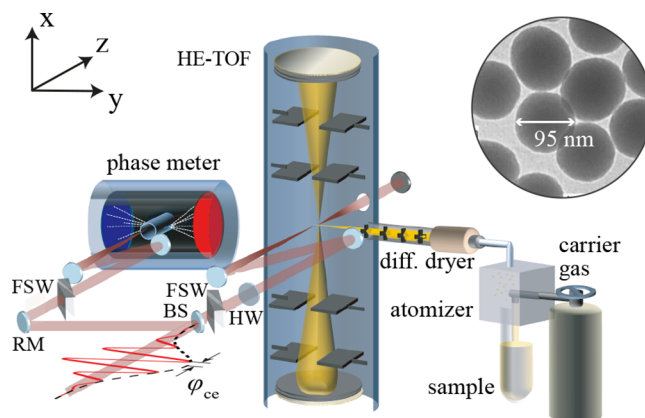


**Figure 1.** Schematic of the experimental setup. Few-cycle laser pulses illuminate isolated SiO<sub>2</sub> nanoparticles. The particles are injected and focused via an aerodynamic lens into the center of a stereographic high-energy time-of-flight (HE-TOF) electron spectrometer. The CEP  $\varphi_{ce}$  of the few-cycle pulses is tagged for each laser shot by a phase meter. The upper right inset shows a transmission electron micrograph of the SiO<sub>2</sub> nanoparticles with a diameter of 95 nm. HW: half-wave plate; RM: reflecting mirror; BS: beam splitter; FSW: fused silica wedges.

released from Xe were recorded in both directions along the polarization axis (which was turned into the horizontal direction by a half-wave plate) with time-of-flight (TOF) spectrometers. The asymmetry between the spectra is used to determine the CEP of a given laser shot. The remainder of the beam was focused into the interaction region of a stereographic high-energy time-of-flight (HE-TOF) electron spectrometer,<sup>21</sup> with the laser polarized along the vertical spectrometer axis ( $x$ -axis), propagating along the  $z$ -axis. A beam of isolated nanospheres was delivered into the laser interaction region by aerodynamic lens focusing.<sup>13,23,40</sup> The nanoparticles were aerosolized by an atomizer with nitrogen from a 2 g/L water dispersion, and the remaining water in the gas stream was removed in an aerosol diffusion dryer.<sup>41</sup> Silica nanoparticles with a 95 nm diameter were prepared at FU Berlin by wet chemistry based on the Stöber procedure<sup>42</sup> and a seeded growth process. Characterization by transmission electron microscopy yielded a polydispersity of less than 10%.<sup>24</sup> The 60 nm diameter ZrO<sub>2</sub> and Si samples were obtained from a commercial supplier (in particular, GmbH). For these samples, the size deviation was around 20%, as communicated by the manufacturer. Spherical Au nanoparticles with an average diameter of 15 nm, a 10% polydispersity, and a plasmon band peaking at 519 nm were synthesized at the Center for NanoScience (LMU Munich) by means of the so-called Turkevich method, which consists of the citrate-assisted reduction of a boiling gold precursor (HAuCl<sub>4</sub>) in water.<sup>43</sup> Despite some variation in the diameters  $d$  of the nanoparticles for different materials, the size parameter  $\rho = \pi d/\lambda$  for all particles remained well below unity, such that scattering in the Rayleigh limit prevails and propagation effects do not play a significant role.<sup>25</sup>

The HE-TOF spectrometer provided a sufficient time resolution to detect electrons with kinetic energies up to about 3 keV at a full opening angle of 20° in both directions. The birth time of the photoelectrons was defined by the detection time of scattered light from the incident few-cycle pulses in the spectrometer. The arrival time of a single electron event was obtained from a peak detection algorithm. The

single-event electron signals from the two TOF signals of the HE-TOF for each laser shot together with two TOF signals from the phase meter were read out by a digitizer (Agilent Acquiris DC271) with a time resolution of 500 ps. In post-analysis, the CEP was determined from the phase meter data, as outlined in refs 44 and 45. The laser peak intensities in the interaction region were characterized from ATI cutoff energies recorded for nitrogen.

## DISCUSSION

In our presentation and discussion of the data, we will first focus on electron emission from 95 nm SiO<sub>2</sub> nanoparticles. For these nanoparticles, data at lower intensities were reported for a variety of sizes and could be quantitatively modeled by semiclassical trajectory simulations,<sup>23–25,35,36</sup> making them ideal model systems. Figure 2a displays the measured intensity-dependent, CEP-averaged  $U_p$ -rescaled electron cutoff energies (black symbols), see the Methods section for details on the determination of the cutoff energy values. For low intensities, the measured cutoffs match the previously reported values near 50  $U_p$ .<sup>23</sup> In contrast, for higher intensity, the cutoff starts to increase around  $I_{\text{trans}} = 1.8 \times 10^{14}$  W/cm<sup>2</sup> (the transition intensity), followed by a saturation near 100  $U_p$ .

To illuminate the physics behind the observed change in cutoff energies, we employ semiclassical Mean-field Mie Monte-Carlo (M<sup>3</sup>C) trajectory simulations, which have been used previously for strong-field electron emission studies<sup>24,25,35,36</sup> as well as attosecond photoionization delays associated with in-medium electron scattering.<sup>34</sup> For technical details, see ref 46. In brief, photoelectrons are generated by evaluating tunnelling rates for the local instantaneous near-field and employing an effective molecular ionization potential. For surface ionization we use  $I_p^{\text{surf}} = 9$  eV, similar to earlier studies<sup>23,24</sup> and as reported in the literature.<sup>47</sup> The time-dependent near-field is constructed from the Mie solution via spectral decomposition, including dispersion and a quasi-instantaneous contribution from generated free charges (conduction electrons and residual ions). Classical electron trajectories are integrated, including a Monte-Carlo sampling of elastic scattering and impact ionization events inside the nanoparticle according to the respective scattering cross sections. Here, we use an improved description of elastic scattering at low electron kinetic energies to resolve the buildup of the plasmonic response from low-energy conduction electrons (see Methods for details).

Figure 2a shows CEP-averaged cutoff energies predicted by M<sup>3</sup>C simulations, including tunnelling at the nanoparticle surface only (dashed blue curve). Note that impact ionization in the volume of the particle is still included. Though this treatment reproduces the experimental cutoffs below the transition intensity, it fails to capture the cutoff evolution for higher intensities. In contrast, simulations with tunnelling in the volume of the particle (hereafter referred to as volume tunnelling) enabled (solid blue curve), reproduce the evolution also for high intensity and suggest a modification of the cutoff energy that is consistent with the experiment. Volume tunnelling is approximated by an atomic ionization rate with an effective ionization potential. Good agreement of the simulation results with the experimental data is found for  $I_p^{\text{vol}} = 11$  eV, noting that the M<sup>3</sup>C simulations cannot account for strong-field induced band gap changes in solids.<sup>46,48</sup> Such effects would likely modify the onset of carrier injection and

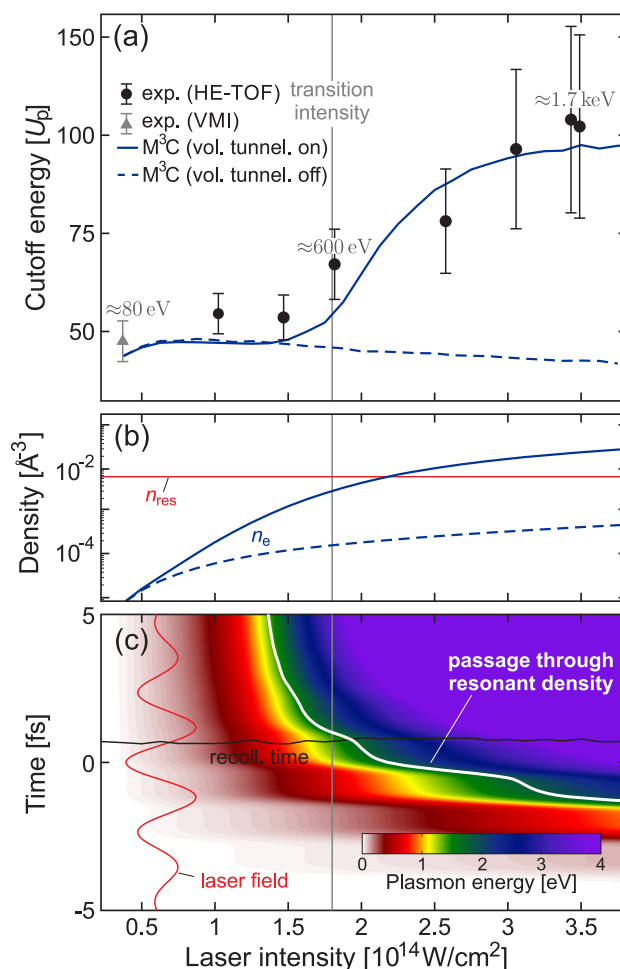


**Figure 2.** (a) Electron cutoff energies (CEP-averaged) measured for 95 nm SiO<sub>2</sub> nanoparticles (black circles) as a function of laser intensity. Error bars represent the TOF timing jitter (<300 ps) and the time resolution of the transient recorder acquisition system (500 ps). The VMI data (gray triangle) is taken from ref 24 and shown for comparison. Blue curves represent cutoffs predicted from M<sup>3</sup>C simulations for the experimental parameters (including focus averaging) with tunnel ionization enabled only at the surface (dashed) and within the full volume (solid). (b) Number density of free electrons  $n_e$  at the pulse peak from M<sup>3</sup>C simulations with and without volume tunneling (as indicated) as a function of intensity. The density for which the frequency of the plasmon matches the laser frequency is indicated as resonant density  $n_{\text{res}}$ . (c) Temporal evolution of the instantaneous plasmon energy, as predicted by M<sup>3</sup>C for  $\varphi_{\text{ce}}=0$  (color coded) vs intensity. Solid white and black curves mark the resonant condition and the recollision time for the fastest electrons, respectively.

avalanche ionization, which is not crucial for the ionization-induced dynamics discussed here.

For a detailed analysis of the evolution and impact of volume tunnelling, we inspect the number density of generated electrons  $n_e$ , the instantaneous plasmon frequency

$\omega_p = \sqrt{\frac{n_{\text{ion}} e^2}{3m_e \epsilon_0}}$  assuming free electrons with mass  $m_e = 9.1 \times 10^{-31}$  kg and equality of the electron density and the density of ion charges  $n_{\text{ion}} = n_e$ , and the resonance ( $\omega_p = \omega_0$ ) realized for  $n_e = n_{\text{res}}$ . For clarity, we like to note that this simplified analysis neglects the influence of the effective electron mass which, however, is expected to not result in qualitative changes regarding the physics. The M<sup>3</sup>C results in Figure 2b reveal that

the plasma remains underdense ( $n \ll n_{\text{res}}$ ) in the investigated intensity range when neglecting volume tunnelling and can reach the transition state only when including volume tunnelling (solid blue curve). Although impact ionization is always evaluated, it is suppressed due to the lack of carriers in the case of disabled volume tunneling. When volume tunneling is included, a rapid increase of the electron density takes place and leads to a situation that enables a metallic response. The fact that metallization near the pulse peak, here defined as crossing of the resonant density, is realized close to the transition intensity, supports that this effect is the essential factor underlying the observed change in electron cutoff energies.

Figure 2c displays the temporal evolution of the plasmon energy (color-coded) as a function of peak intensity for the full M<sup>3</sup>C simulations. The ionization-induced blue-shift of the plasmon becomes increasingly pronounced at higher intensities, resulting in a systematic shift of the resonance point toward the leading edge of the pulse (solid white curve). Well below the transition intensity, ionization is weak and the system remains underdense at all times. In the vicinity of the transition intensity, the resonant density is reached around the pulse maximum, where the timing coincides closely with the recollision time of the fastest electrons (see solid black curve). Finally, for intensities above the transition intensity, the metallization occurs prior to the recollision of cutoff electrons such that the relevant part of their acceleration process takes place in an overdense plasma state. In this latter case, the sphere's polarization response can be approximated by that of a perfectly conducting small sphere, where internal fields are screened and a surface intensity enhancement of 9 is expected at the poles, leading to a classical electron backscattering cutoff of  $90 U_p$ .<sup>49</sup> The observation of slightly higher cutoffs is attributed to the additional charge interaction, as mentioned above.

For a microscopic analysis of the acceleration process, Figure 3a,b shows the simulated spatiotemporal evolution of both the near-fields at the sphere's surface in the upper pole region and the averaged trajectories of electrons with final energies close to the respective cutoffs for two different intensities. Below the transition intensity (Figure 3a,c), the fields inside and outside exhibit a jump in the normal component due to the dielectric enhancement but maintain similar signs and phases in the relevant stages of the evolution. In contrast, above the transition intensity (Figure 3b,d), the near-field is strongly modified for  $t \gtrsim -0.5$  fs, manifesting in three distinct features. First, the inside and outside fields run out of phase (black vs green curve in Figure 3d). Second, the inside field starts to decay substantially and is finally almost perfectly screened for  $t \gtrsim 2.5$  fs within roughly one optical cycle, indicating the ultrafast transition to a metallic state. Third, the magnitude of the outside field (green curve in Figure 3d) is substantially enhanced, assisting the electron acceleration process via the resulting higher energy gain in the backscattering process. The coincidence of these near-field modifications, particularly the enhancement of the outside field, with the passage through the resonant density (cf. Figure 3f in contrast to Figure 3e) provides the link between the ultrafast metallization and the observed change in the  $U_p$ -rescaled electron cutoff energies. Metallization of the whole particle volume above the transition intensity is further supported by the radial density profile of plasma electrons during the recollision phase, see blue curves in Figure 3g. Below the transition intensity, free electrons are

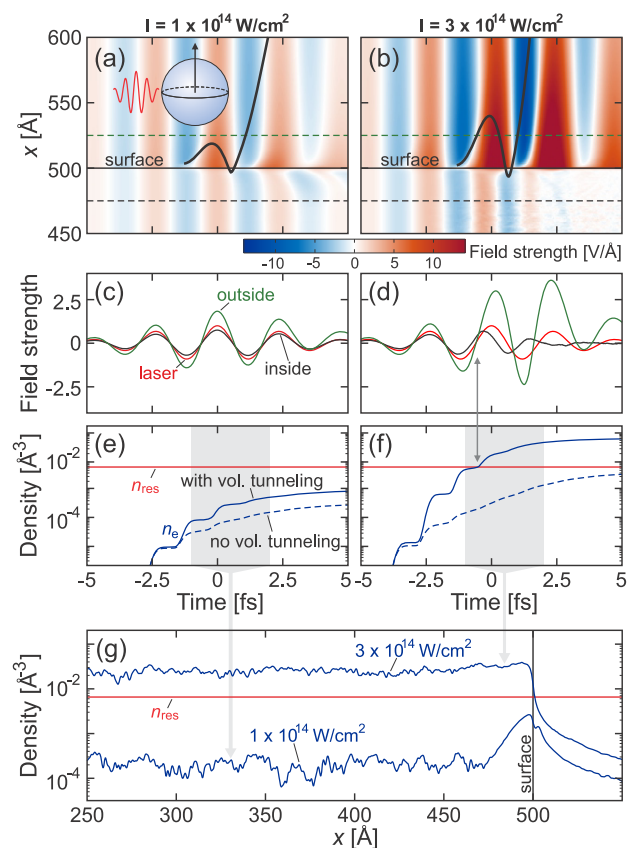


**Figure 3.** (a, b) Evolution of the normal component of the internal ( $x < 500$  Å) and external ( $x > 500$  Å) near-fields at the surface of SiO<sub>2</sub> nanospheres evaluated along the polarization axis (cf. black arrow in the pictogram in panel (a)) under few-cycle NIR laser pulses at  $\varphi_{\text{ce}} = 0$  for two different intensities (as indicated). Solid black curves show averaged trajectories of the fastest ten percent of emitted electrons. (c, d) Field strengths along the cuts indicated by the respective dashed lines in (a) and (b), normalized to the peak of the laser field (red curve). (e, f) Evolution of the number density of generated electrons from simulations without (dashed) and with (solid) volume tunneling. Note that impact ionization is included in both cases. The red line indicates the electron density at resonance ( $n_{\text{res}}$ ). (g) Electron density along the  $x$ -axis around the upper pole (cf. black arrow in the inset in panel (a)) calculated with volume tunneling for both intensities and averaged during the recollision phase (gray areas in (e) and (f)).

localized near the surface as they result mainly from surface tunneling and show a rapid density decrease inside the nanoparticle. Even in the density peak, the electron density remains below the resonant density. In contrast, the metallization above the transition intensity induces a nearly homogeneous free electron density distribution inside the particle with a density value that exceeds the resonant density. The fact that the profile shows a sharp density step at the surface further supports the picture of the formation of a nearly perfect metal-like sphere. Hence, the comparison of the density profiles for low and high intensity in Figure 3g provides an intuitive picture of the nanoplasma formation process.

The M<sup>3</sup>C simulations show that fast electrons, especially those in the cutoff region, result from field-driven electron backscattering in all considered cases. We like to note that these electrons reach their energies within a fraction of the laser pulse duration, which makes them particularly suited as a decisive marker for the ionization-induced metallization. To

strengthen our claim that field-driven electrons dominate the observed behavior, we compare simulated CEP-dependent asymmetry features of the electron emission with the experimental data. We analyze the energy-dependent electron yields  $Y_{\text{up}}$  and  $Y_{\text{down}}$ , which correspond to emission into the up- and downward directions along the laser polarization axis and determine the asymmetry parameter  $Y_{\text{asym}} = (Y_{\text{up}} - Y_{\text{down}})/(Y_{\text{up}} + Y_{\text{down}})$  from the simulated and experimental data. Figure 4a,c

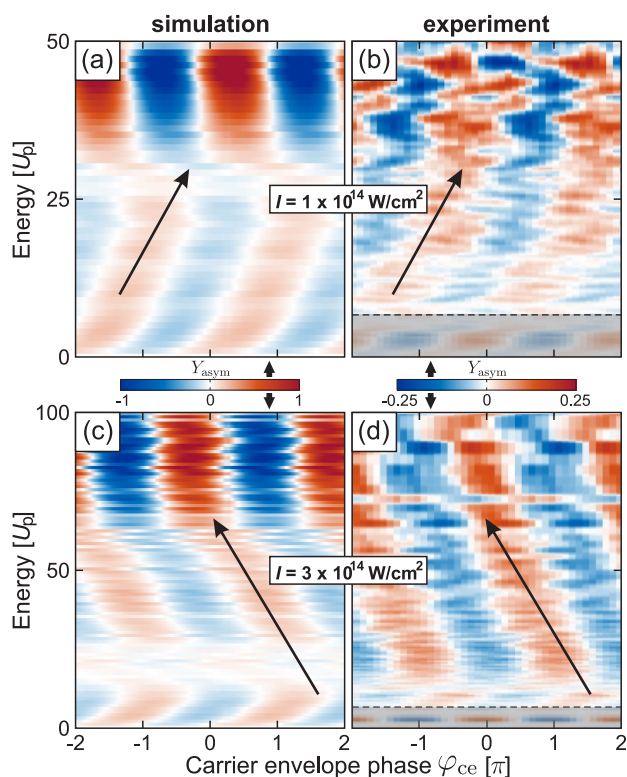


**Figure 4.** (a, c) Energy- and CEP-dependent asymmetry maps of recollision electrons emitted from 95 nm  $\text{SiO}_2$  nanospheres for two laser intensities (as indicated) from  $M^3C$  simulations for the experimental parameters of this study (including focal volume averaging). (b, d) Corresponding asymmetry maps obtained from the experimental data. Note that the experimental maps are contaminated with background gas signal at low energies (gray shaded area). Black arrows indicate the different tilts of the asymmetry features observed below (a, b) and above (c, d) the transition intensity.

presents the resulting energy- and CEP-resolved asymmetry maps from  $M^3C$  simulations for the same peak intensities as considered before in Figure 3. The representative example below the transition intensity exhibits an asymmetry pattern that shows a pronounced tilt to increased CEP values with energy (i.e., a right-tilt in Figure 4a, see eye-guiding black arrow), which is consistent with results from previous studies.<sup>23,24</sup> This trend is different from the behavior predicted above the transition intensity, where a tilt with decreasing CEP values for increasing energy (i.e., a left-tilt, see black arrow in Figure 4c) is seen. The change of the tilt behavior for the intermediate energy range is attributed to a change of the relevant part of the pulse that generates the corresponding electron signal. While a right-tilted feature is associated with dominance of the trailing edge, a left-tilted feature follows for a dominance of the leading pulse edge. The behavior thus supports that electrons with intermediate energies mostly

emerge in the leading pulse edge for high intensity. The tilt features are also found in the experimental asymmetry maps, see Figure 4b,d, supporting that the model not only reproduces the cutoff energies, but also correctly captures the dynamics of the subcycle electron acceleration.

The experimental and theoretical results for the dielectric  $\text{SiO}_2$  nanoparticles motivate the question if the observed behavior is of general nature for initially nonmetallic materials and how this compares to an initially metallic system. We have thus additionally investigated nanoparticles of different material classes: dielectrics ( $\text{SiO}_2$ ,  $\text{ZrO}_2$ ), a semiconductor (Si), and a metal (Au). Figure 5 shows the experimental electron

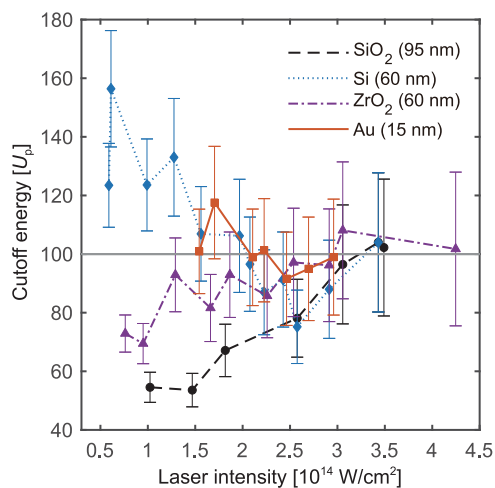


**Figure 5.** Experimentally obtained  $U_p$ -rescaled electron cutoff energies  $E_c/U_p$  as a function of incident laser intensity for different nanoparticles.

cutoff-energies ( $E_c$ ) for these different materials, where it can be seen that the cutoff values for dielectric and semiconducting particles with increasing intensity converge to that of the metallic particles. The Au sample shows values of  $E_c$  between 90 and 120  $U_p$ , where due to weaker signals in the experiments, only a limited intensity range could be analyzed. Above  $2.5 \times 10^{14} \text{ W/cm}^2$  all cutoff energies show a similar value around 100  $U_p$  within their respective error bars (indicated as a gray line). It is worth noting that, in the case of the semiconducting Si particles, the cutoff values are actually initially higher (with around 150  $U_p$ ) and decreasing upon metallization. While our comparison to  $M^3C$  simulations has been restricted to  $\text{SiO}_2$ , where reliable simulations can be performed, we assume that a similar ionization-induced metallization at intensities high enough to ignite avalanching in the volume of the particles is responsible for the observed behavior in other materials. The ionization-induced subcycle metallization therefore appears as a general phenomenon.

## CONCLUSIONS

In conclusion, CEP-controlled photoemission in few-cycle pulses in conjunction with semiclassical transport simulations have revealed the ultrafast metallization of nanoparticles. The rapid increase of free electron density inside the particles for intensities high enough to ignite avalanching in the volume of the particles, results in a universal modification of  $U_p$ -rescaled electron cutoff energies to around 100  $U_p$ , independent of the original material. Near-field driven elastic backscattering on the surface of the dynamically metallizing targets was identified as

the underlying mechanism for this observation, and we identify the modification of the electron cutoff energy as the smoking gun for the metallization. We verify the absence of a pronounced resonant near-field enhancement during the ultrafast passage of the resonant density. The associated physics is not limited to nanoparticles and is anticipated to reflect the evolution relevant for other nanotargets, thin films, or even at the surface of solids. In contrast to previous studies below the optical damage threshold,<sup>6</sup> here, we were able to investigate strong-field dynamics at a higher intensity, where impact ionization seeded by initial tunneling takes place. Our protocol, that is, a switching behavior in the electron cutoff energy and CEP-dependent asymmetry, opens up new avenues for tracing strong-field dynamics in nanosystems under extreme conditions on the single-cycle time scale.

## METHODS

**Cutoff Determination.** The cutoffs in the photoelectron kinetic energy spectra were obtained from the CEP averaged TOF spectra. Figure 6 shows a typical TOF spectrum for a

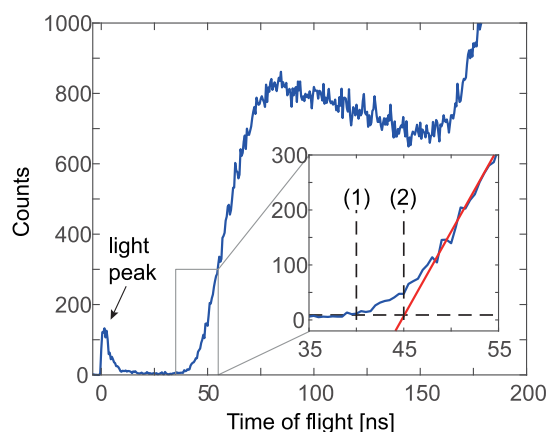


**Figure 6.** Time-of-flight spectrum of a measurement on SiO<sub>2</sub> nanoparticles at an intensity of  $1.5 \times 10^{14}$  W/cm<sup>2</sup>. The inset illustrates the two methods for determining the cutoff.

SiO<sub>2</sub> nanoparticle measurement. The small peak close to zero delay time is produced by laser light, and exhibits a long exponential tail. Two methods were used to obtain the cutoff energies. In the first one, the cutoff is defined as the position in the TOF spectrum where the signal reaches the noise level (indicated by (1) in the inset of Figure 6). Due to the low signal-to-noise ratio in the cutoff region, and especially the overlap between the short flight times for high-energy electrons and the light peak at high laser intensities, the exact cutoff energy cannot be assigned unambiguously by this method. The TOF spectrum, however, shows a nearly linear decay in the higher energy range (shorter flight time). This feature permits a cutoff by fitting the spectrum linearly, as indicated by (2) in the inset of Figure 6. The final cutoff energy was obtained from averaging the results of both methods. The trigger jitter and digitizer resolution were taken into account as systematic errors, reflected in the error bars in Figures 2 and 5 of the main text.

**Low-Energy Elastic Scattering.** Within the M<sup>3</sup>C model (for details, see ref 46), both elastic and inelastic electron–atom collisions are included via Monte Carlo sampling of the respective energy-dependent scattering cross sections. In each numerical time step, the realization of scattering events is

tested for all electron trajectories residing in the sphere volume. In the current simulations we adapted the elastic scattering, while the inelastic scattering remained as in previous work.<sup>24,34</sup> The rationale is as follows: In earlier studies (strong-field ionization far below the turnover intensity<sup>24</sup> and attosecond streaking<sup>34</sup>), we considered atomic scattering cross sections for the elastic collisions that were obtained from quantum scattering simulations using the atomic potentials (of silicon and oxygen). The individual atomic results are converted to transport cross sections and combined according to the stoichiometric ratios (2-to-1) to construct an effective molecular transport cross section  $\sigma_{\text{el}}^{\text{trans}}$  for SiO<sub>2</sub>. Such a description overestimates the scattering probability at low electron energies, as solid state effects, including the finite size of the Wigner-Seitz cell, are neglected. In particular, the effective molecular cross section can become larger than the geometrical cross section  $\sigma_{\text{geo}} = n^{-2/3}$  of the molecular Wigner-Seitz cell (compare dashed black curve and horizontal gray line in Figure 7). Here  $n = 0.022 \text{ \AA}^{-3}$  is the number

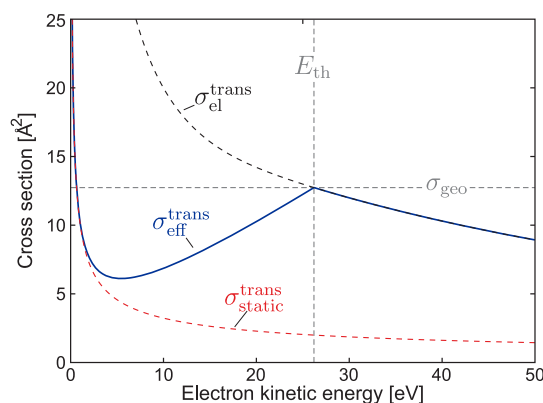


**Figure 7.** Energy-dependent effective transport cross section for elastic scattering in SiO<sub>2</sub> (solid blue curve). The dashed black and red curves represent the effective molecular transport cross section (as used in previous studies, see e.g., ref 34) and a static cross section corresponding to a constant collision frequency, respectively. The horizontal dashed line indicates the geometric cross section of the Wigner-Seitz cell and the vertical dashed line marks the threshold energy, where molecular and geometric cross sections are equal.

density of scattering centers (effective SiO<sub>2</sub> molecules). For all scenarios considered so far, where scattering of low energy electrons was of minor importance for the relevant observables, the above description was sufficient. However, it fails to capture the buildup of collective oscillations of liberated slow electrons in the driving laser field (Mie plasmon) emerging from extensive volume tunneling.

Therefore, we consider an energy-dependent effective transport cross section

$$\sigma_{\text{eff}}^{\text{trans}} = \begin{cases} \sigma_{\text{stat}}^{\text{trans}} \left( 1 - \frac{E}{E_{\text{th}}} \right) + \sigma_{\text{geo}} \frac{E}{E_{\text{th}}} & \text{for } E \leq E_{\text{th}} \\ \sigma_{\text{el}}^{\text{trans}} & \text{for } E > E_{\text{th}}, \end{cases}$$

see solid blue curve in Figure 7. Below the threshold energy  $E_{\text{th}}$ , where  $\sigma_{\text{el}}^{\text{trans}} = \sigma_{\text{geo}}$  (vertical dashed line), the effective cross section is given by a linear mixture of the geometric area  $\sigma_{\text{geo}}$  and a cross section  $\sigma_{\text{static}} = (\nu n \tau)^{-1}$ , which mimics an energy independent collision frequency  $\tau^{-1}$  ( $\nu$  is the electron

velocity). In the low velocity limit, this model describes a fixed lifetime  $\tau$  of plasmonic excitations, which is typically of the order of one fs (cf. red dashed curve). We used a value of  $\tau = 750$  as and checked that the key signatures are robust against slight variations of this value. Above  $E_{th}$ , we employ the conventional model and use the effective molecular transport cross section. As a result, the high energy description remains unchanged and is matched in a continuous way to a low energy limit of constant lifetime.

## AUTHOR INFORMATION

### Corresponding Authors

**Thomas Fennel** – Institute for Physics and Department of Life, Light and Matter, University of Rostock, 18051 Rostock, Germany; Max-Born-Institute, 12489 Berlin, Germany; Email: [thomas.fennel@uni-rostock.de](mailto:thomas.fennel@uni-rostock.de)

**Matthias F. Kling** – Max Planck Institute of Quantum Optics, 85748 Garching, Germany; Department of Physics, Ludwig-Maximilians-Universität Munich, 85748 Garching, Germany; Center for Advanced Laser Applications, 85748 Garching, Germany; [orcid.org/0000-0002-1710-0775](https://orcid.org/0000-0002-1710-0775); Email: [matthias.kling@lmu.de](mailto:matthias.kling@lmu.de)

### Authors

**Qingcao Liu** – Max Planck Institute of Quantum Optics, 85748 Garching, Germany; Department of Physics, Ludwig-Maximilians-Universität Munich, 85748 Garching, Germany

**Lennart Seiffert** – Institute for Physics, University of Rostock, 18051 Rostock, Germany

**Frederik Süßmann** – Max Planck Institute of Quantum Optics, 85748 Garching, Germany; Department of Physics, Ludwig-Maximilians-Universität Munich, 85748 Garching, Germany

**Sergey Zherebtsov** – Max Planck Institute of Quantum Optics, 85748 Garching, Germany; Department of Physics, Ludwig-Maximilians-Universität Munich, 85748 Garching, Germany

**Johannes Passig** – Institute for Physics and Department of Life, Light and Matter, University of Rostock, 18051 Rostock, Germany; [orcid.org/0000-0002-3876-1716](https://orcid.org/0000-0002-3876-1716)

**Alexander Kessel** – Max Planck Institute of Quantum Optics, 85748 Garching, Germany

**Sergei A. Trushin** – Max Planck Institute of Quantum Optics, 85748 Garching, Germany

**Nora G. Kling** – Max Planck Institute of Quantum Optics, 85748 Garching, Germany; J. R. Macdonald Laboratory, Department of Physics, Kansas State University, Manhattan, Kansas 66506, United States

**Itzik Ben-Itzhak** – J. R. Macdonald Laboratory, Department of Physics, Kansas State University, Manhattan, Kansas 66506, United States

**Valerie Mondes** – Physical Chemistry, Freie Universität Berlin, 14195 Berlin, Germany

**Christina Graf** – Department of Chemistry and Biotechnology, Darmstadt University of Applied Sciences, 64295 Darmstadt, Germany; [orcid.org/0000-0002-3308-5640](https://orcid.org/0000-0002-3308-5640)

**Eckart Rühl** – Physical Chemistry, Freie Universität Berlin, 14195 Berlin, Germany; [orcid.org/0000-0002-0451-8734](https://orcid.org/0000-0002-0451-8734)

**Laszlo Veisz** – Department of Physics, Umeå University, 90187 Umeå, Sweden

**Stefan Karsch** – Department of Physics, Ludwig-Maximilians-Universität Munich, 85748 Garching, Germany; Center for Advanced Laser Applications, 85748 Garching, Germany

**Jessica Rodríguez-Fernández** – Department of Physics and CeNS, Ludwig-Maximilians-Universität, 80539 Munich, Germany

**Mark I. Stockman** – Physics Department, Georgia State University, Atlanta, Georgia 30303, United States

**Josef Tiggesbäumker** – Institute for Physics and Department of Life, Light and Matter, University of Rostock, 18051 Rostock, Germany; [orcid.org/0000-0002-2027-3001](https://orcid.org/0000-0002-2027-3001)

**Karl-Heinz Meiwes-Broer** – Institute for Physics and Department of Life, Light and Matter, University of Rostock, 18051 Rostock, Germany

Complete contact information is available at:

<https://pubs.acs.org/10.1021/acsp Photonics.0c01282>

### Author Contributions

Q.L. and L.S. contributed equally to this work.

### Notes

The authors declare no competing financial interest.

## ACKNOWLEDGMENTS

We thank F. Krausz and J. Feldmann for their support and fruitful discussions. We are grateful for support by the Max Planck Society, by the China Scholarship Council, by the German Research Foundation (DFG) via SPP1840 and SFB652. S.Z. was supported from the DFG via ZH582/1-1. J.T. acknowledges financial support from the DFG (TI210-7/1, TI210-8/1). L.V. acknowledges the support by the grants from the Swedish Research Council (2016-05409 and 2019-02376). MIS support was provided by Grant No. DE-FG02-01ER15213 from the Atomic, Molecular and Optical Sciences Program, Office of Basic Energy Sciences, the U.S. Department of Energy. I.B.I. acknowledges support from the same funding agency, Grant No. DE-FG02-86ER13491. E.R. acknowledges financial support by the BMBF (Grant 05K16KEA). T.F. acknowledges additional financial support from the DFG via a Heisenberg-Grant (ID: 398382624) and from the Bundesministerium für Bildung und Forschung (BMBF, ID: 05K16HRB). Computing time has been provided by the North German Supercomputing Alliance (HLRN, ID: mvp00013).

## REFERENCES

- (1) Luu, T. T.; Garg, M.; Kruchinin, S. Y.; Moulet, A.; Hassan, M. T.; Goulielmakis, E. Extreme ultraviolet high-harmonic spectroscopy of solids. *Nature* **2015**, *521*, 498–502.
- (2) Han, S.; Kim, H.; Kim, Y. W.; Kim, Y.-J.; Kim, S.; Park, I.-Y.; Kim, S.-W. *Nat. Commun.* **2016**, *7*, 13105.
- (3) Durach, M.; Rusina, A.; Kling, M. F.; Stockman, M. I. Predicted Ultrafast Dynamic Metallization of Dielectric Nanofilms by Strong Single-Cycle Optical Fields. *Phys. Rev. Lett.* **2011**, *107*, 086602.
- (4) Schultze, M.; Bothschafter, E. M.; Sommer, A.; Holzner, S.; Schweinberger, W.; Fiess, M.; Hofstetter, M.; Kienberger, R.; Apalkov, V.; Yakovlev, V. S.; Stockman, M. I.; Krausz, F. Controlling dielectrics with the electric field of light. *Nature* **2013**, *493*, 75–78.
- (5) Schultze, M.; Ramasesha, K.; Pemmaraju, C.; Sato, S.; Whitmore, D.; Gandman, A.; Prell, J. S.; Borja, L. J.; Prendergast, D.; Yabana, K.; Neumark, D. M.; Leone, S. R. Attosecond band-gap dynamics in silicon. *Science* **2014**, *346*, 1348–1352.
- (6) Schiffrin, A.; et al. Optical-field-induced current in dielectrics. *Nature* **2013**, *493*, 70–74.
- (7) Krausz, F.; Stockman, M. I. Attosecond metrology: from electron capture to future signal processing. *Nat. Photonics* **2014**, *8*, 205–213.
- (8) Schötz, J.; Wang, Z.; Pisanty, E.; Lewenstein, M.; Kling, M. F.; Ciappina, M. *ACS Photonics* **2019**, *6*, 3057–3069.

- (9) Englert, L.; Wollenhaupt, M.; Haag, L.; Sarpe-Tudoran, C.; Rethfeld, B.; Baumert, T. Material processing of dielectrics with temporally asymmetric shaped femtosecond laser pulses on the nanometer scale. *Appl. Phys. A: Mater. Sci. Process.* **2008**, *92*, 749–753.
- (10) Balling, P.; Schou, J. Femtosecond-laser ablation dynamics of dielectrics: basics and applications for thin films. *Rep. Prog. Phys.* **2013**, *76*, 036502.
- (11) Jürgens, P.; Liewehr, B.; Kruse, B.; Peltz, C.; Engel, D.; Husakou, A.; Witting, T.; Ivanov, M.; Vrakking, M. J. J.; Fennel, T.; Mermillod-Blondin, A. Origin of strong-field induced low-order harmonic generation in amorphous solids. *Nat. Phys.* **2020**, *16*, 1035.
- (12) Ditmire, T.; Smith, R. A.; Tisch, J. W. G.; Hutchinson, M. H. R. High Intensity Laser Absorption by Gases of Atomic Clusters. *Phys. Rev. Lett.* **1997**, *78*, 3121–3124.
- (13) Hickstein, D. D.; Dollar, F.; Gaffney, J. A.; Foord, M. E.; Petrov, G. M.; Palm, B. B.; Keister, K. E.; Ellis, J. L.; Ding, C.; Libby, S. B.; Jimenez, J. L.; Kapteyn, H. C.; Murnane, M. M.; Xiong, W. Observation and Control of Shock Waves in Individual Nanoplasmas. *Phys. Rev. Lett.* **2014**, *112*, 115004.
- (14) Rose-Petruck, C.; Schafer, K. J.; Wilson, K. R.; Barty, C. P. J. Ultrafast electron dynamics and inner-shell ionization in laser driven clusters. *Phys. Rev. A: At., Mol., Opt. Phys.* **1997**, *55*, 1182–1190.
- (15) Saalman, U.; Siedschlag, C.; Rost, J. M. Mechanisms of cluster ionization in strong laser pulses. *J. Phys. B: At., Mol. Opt. Phys.* **2006**, *39*, R39–R77.
- (16) Fennel, T.; Meiwes-Broer, K.-H.; Tiggesbäumker, J.; Reinhard, P.-G.; Dinh, P. M.; Surau, E. Laser-driven nonlinear cluster dynamics. *Rev. Mod. Phys.* **2010**, *82*, 1793–1842.
- (17) Cardenas, D. E.; Ostermayr, T. M.; Di Lucchio, L.; Hofmann, L.; Kling, M. F.; Gibbon, P.; Schreiber, J.; Veisz, L. Sub-cycle dynamics in relativistic nanoplasma acceleration. *Sci. Rep.* **2019**, *9*, 7321.
- (18) Döppner, T.; Müller, J. P.; Przystawik, A.; Göde, S.; Tiggesbäumker, J.; Meiwes-Broer, K.-H.; Varin, C.; Ramunno, L.; Brabec, T.; Fennel, T. Steplike Intensity Threshold Behavior of Extreme Ionization in Laser-Driven Xenon Clusters. *Phys. Rev. Lett.* **2010**, *105*, 053401.
- (19) Schütte, B.; Arbeiter, M.; Mermillod-Blondin, A.; Vrakking, M. J. J.; Rouzée, A.; Fennel, T. Ionization Avalanching in Clusters Ignited by Extreme-Ultraviolet Driven Seed Electrons. *Phys. Rev. Lett.* **2016**, *116*, 033001.
- (20) Fennel, T.; Döppner, T.; Passig, J.; Schaal, C.; Tiggesbäumker, J.; Meiwes-Broer, K.-H. Plasmon-Enhanced Electron Acceleration in Intense Laser Metal-Cluster Interactions. *Phys. Rev. Lett.* **2007**, *98*, 143401.
- (21) Passig, J.; Zherebtsov, S.; Irsig, R.; Arbeiter, M.; Peltz, C.; Goede, S.; Skruszewicz, S.; Meiwes-Broer, K.-H.; Tiggesbäumker, J.; Kling, M. F.; Fennel, T. Nanoplasmonic electron acceleration by attosecond-controlled forward rescattering in silver clusters. *Nat. Commun.* **2017**, *8*, 1181.
- (22) Ciappina, M. F.; et al. Attosecond physics at the nanoscale. *Rep. Prog. Phys.* **2017**, *80*, 054401.
- (23) Zherebtsov, S.; et al. Controlled near-field enhanced electron acceleration from dielectric nanospheres with intense few-cycle laser fields. *Nat. Phys.* **2011**, *7*, 656–662.
- (24) Zherebtsov, S.; et al. Carrier-envelope phase-tagged imaging of the controlled electron acceleration from SiO<sub>2</sub> nanospheres in intense few-cycle laser fields. *New J. Phys.* **2012**, *14*, 075010.
- (25) Süßmann, F.; et al. Field propagation-induced directionality of carrier-envelope phase-controlled photoemission from nanospheres. *Nat. Commun.* **2015**, *6*, 7944.
- (26) Rupp, P.; et al. Quenching of material dependence in few-cycle driven electron acceleration from nanoparticles under many-particle charge interaction. *J. Mod. Opt.* **2017**, *64*, 995–1003.
- (27) Krüger, M.; Schenk, M.; Hommelhoff, P. Attosecond control of electrons emitted from a nanoscale metal tip. *Nature* **2011**, *475*, 78–81.
- (28) Herink, G.; Solli, D.; Gulde, M.; Ropers, C. Field-driven photoemission from nanostructures quenches the quiver motion. *Nature* **2012**, *483*, 190–193.
- (29) Piglosiewicz, B.; Schmidt, S.; Park, D. J.; Vogelsang, J.; Grosz, P.; Manzoni, C.; Farinello, P.; Cerullo, G.; Lienau, C. Carrier-envelope phase effects on the strong-field photoemission of electrons from metallic nanostructures. *Nat. Photonics* **2014**, *8*, 37–42.
- (30) Vogelsang, J.; Robin, J.; Nagy, B. J.; Dombi, P.; Rosenkranz, D.; Schiek, M.; Groß, P.; Lienau, C. Ultrafast Electron Emission from a Sharp Metal Nanotaper Driven by Adiabatic Nanofocusing of Surface Plasmons. *Nano Lett.* **2015**, *15*, 4685–4691.
- (31) Yanagisawa, H.; Schnepf, S.; Hafner, C.; Hengsberger, M.; Kim, D.; Kling, M. F.; Landsman, A.; Gallmann, L.; Osterwalder, J. Delayed electron emission channel in strong-field driven tunneling from a metallic nanotip. *Sci. Rep.* **2016**, *6*, 35877.
- (32) Schötz, J.; Mitra, S.; Fuest, H.; Neuhaus, M.; Okell, W. A.; Förster, M.; Paschen, T.; Ciappina, M. F.; Yanagisawa, H.; Wnuk, P.; Hommelhoff, P.; Kling, M. F. Nonadiabatic ponderomotive effects in photoemission from nanotips in intense midinfrared laser fields. *Phys. Rev. A: At., Mol., Opt. Phys.* **2018**, *97*, 013413.
- (33) Dombi, P.; Hörl, A.; Rác, P.; Márton, I.; Trügler, A.; Krenn, J. R.; Hohenester, U. Ultrafast Strong-Field Photoemission from Plasmonic Nanoparticles. *Nano Lett.* **2013**, *13*, 674–678.
- (34) Seiffert, L.; et al. Attosecond chronoscopy of electron scattering in dielectric nanoparticles. *Nat. Phys.* **2017**, *13*, 766–770.
- (35) Seiffert, L.; Süßmann, F.; Zherebtsov, S.; Rupp, P.; Peltz, C.; Rühl, E.; Kling, M. F.; Fennel, T. Competition of single and double rescattering in the strong-field photoemission from dielectric nanospheres. *Appl. Phys. B: Lasers Opt.* **2016**, *122*, 101.
- (36) Seiffert, L.; Henning, P.; Rupp, P.; Zherebtsov, S.; Hommelhoff, P.; Kling, M. F.; Fennel, T. Trapping field assisted backscattering in strong-field photoemission from dielectric nanospheres. *J. Mod. Opt.* **2017**, *64*, 1096–1103.
- (37) Ahmad, I.; Bergé, L.; Major, Z.; Krausz, F.; Karsch, S.; Trushin, S. A. Redshift of few-cycle infrared pulses in the filamentation regime. *New J. Phys.* **2011**, *13*, 093005.
- (38) Wittmann, T.; Horvath, B.; Helml, W.; Schätzel, M. G.; Gu, X.; Cavalieri, A. L.; Paulus, G. G.; Kienberger, R. Single-shot carrier-envelope phase measurement of few-cycle laser pulses. *Nat. Phys.* **2009**, *5*, 357–362.
- (39) Johnson, N. G.; et al. Single-shot carrier-envelope-phase-tagged ion-momentum imaging of nonsequential double ionization of argon in intense 4-fs laser fields. *Phys. Rev. A: At., Mol., Opt. Phys.* **2011**, *83*, 013412.
- (40) Wilson, K. R.; Zou, S.; Shu, J.; Rühl, E.; Leone, S. R.; Schatz, G. C.; Ahmed, M. Size-Dependent Angular Distributions of Low-Energy Photoelectrons Emitted from NaCl Nanoparticles. *Nano Lett.* **2007**, *7*, 2014–2019.
- (41) Liu, Q.; Seiffert, L.; Trabattini, A.; Castrovilli, M. C.; Galli, M.; Rupp, P.; Frassetto, F.; Poletto, L.; Nisoli, M.; Rühl, E.; Krausz, F.; Fennel, T.; Zherebtsov, S.; Calegari, F.; Kling, M. F. Attosecond streaking metrology with isolated nanotargets. *J. Opt.* **2018**, *20*, 024002.
- (42) Stöber, W.; Fink, A.; Bohn, E. Controlled growth of monodisperse silica spheres in the micron size range. *J. Colloid Interface Sci.* **1968**, *26*, 62–69.
- (43) Turkevich, J.; Stevenson, P. C.; Hillier, J. A study of the nucleation and growth processes in the synthesis of colloidal gold. *Discuss. Faraday Soc.* **1951**, *11*, 55–75.
- (44) Sayler, A. M.; Rathje, T.; Müller, W.; Rühle, K.; Kienberger, R.; Paulus, G. G. Precise, real-time, every-single-shot, carrier-envelope phase measurement of ultrashort laser pulses. *Opt. Lett.* **2011**, *36*, 1–3.
- (45) Rathje, T.; Johnson, N. G.; Möller, M.; Süßmann, F.; Adolph, D.; Kübel, M.; Kienberger, R.; Kling, M. F.; Paulus, G. G.; Sayler, A. M. Review of attosecond resolved measurement and control via carrier-envelope phase tagging with above-threshold ionization. *J. Phys. B: At., Mol. Opt. Phys.* **2012**, *45*, 074003.

(46) Seiffert, L. Semi-classical description of near-field driven attosecond photoemission from nanostructures. *Ph.D. Thesis*, Rostock University, 2018.

(47) Tashmukhamedova, D. A.; Yusupjanova, M. B. Emission and optical properties of SiO<sub>2</sub>/Si thin films. *J. Surf. Invest.: X-Ray, Synchrotron Neutron Tech.* **2016**, *10*, 1273–1275.

(48) Kwon, O.; Paasch-Colberg, T.; Apalkov, V.; Kim, B.-K.; Kim, J.-J.; Stockman, M. I.; Kim, D. Semimetallization of dielectrics in strong optical fields. *Sci. Rep.* **2016**, *6*, 21272.

(49) Paulus, G. G.; Becker, W.; Nicklich, W.; Walther, H. Rescattering effects in above-threshold ionization: a classical model. *J. Phys. B: At., Mol. Opt. Phys.* **1994**, *27*, L703–L708.